Development of Silicon Probe With Acute Study on *In Vivo* Neural Recording and Implantation Behavior Monitored by Integrated Si-Nanowire Strain Sensors

Songsong Zhang, Shih-Cheng Yen, Zhuolin Xiang, Lun-De Liao, Dim-Lee Kwong, *Fellow, IEEE*, and Chengkuo Lee, *Member, IEEE*

***Abstract*— The silicon probe with highly P-doped Si electrodes was realized on 8-in Silicon on insulator wafer through standard Complementary metal-oxide semiconductor process. By leveraging the same thin Si device layer (∼100 nm), the built-in piezoresistive Si-nanowires (SiNWs) configured in full-bridge structure were also equipped along the probe shank for strain sensing. After additional coatings of nanocomposite (Carbon nanotubes + Au nanoparticles) on silicon electrodes, the functionality of neural recording was validated with a low noise level (<20 μV) during *in vivo* neural recording on rat brain (CA1 region). The additional capability of monitoring probe mechanical behavior was first verified through the probe buckling experiments and further examined with implantations on rat brain (S1 region). Besides the large buckling mechanics, the physiological brain micromotion (e.g., caused by respiration) was successfully picked up by integrated SiNWs strain sensors, which would provide the research platform to practically understand the correlation between the electrical neural signal and the brain micromotion. [2014-0370]**

***Index Terms*— Silicon neural probe, silicon nanowires (SiNWs), neural recording, nano-composite, brain micro-motion.**

I. Introduction

TAKING advantages of standardized processing flows and improved fabrication accuracy [1], the silicon based neural probe has been replacing the traditional metallic counterpart [2] and equipped with extra built-in functions (e.g. multi-functional electrodes and embedded fluidic channels) [3]–[6]. Tremendous researching endeavours have been devoted for both bio-compatibility and mechanical stability of the silicon neural electrode probe over chronic studies [7]–[9]. Meanwhile, the re-configuration of device structure and dimension has been proposed for less tissue damages [10], [11]. In addition, the density of electrodes within single probe shank demands to be largely increased for a higher resolution neuron signal mapping [12]–[14]. Both aforementioned concerns are leading to not only the probe downsizing, but also the reduction of electrode dimension, which will cause the severe degradation for the quality of recorded neural information (e.g. neuron active potentials) against the background noise. In order to boost charge storage capacity (CSC) within a limited electrode area, emerging materials (such as platinum gray [15], activated iridium oxide film (AIROF) [16], conductive polymers [17], [18], various nano-scale materials [19]–[21] and even graphene [22] are reported to be deposited on top of conventional metallic electrodes for CSC.

Meanwhile, integrated circuits (IC) including real-time processing and pre-amplifying functions are also widely deployed for further obtaining qualified neural signals [23], [24], [25]. Moreover, it has also become increasingly clear that the understanding of neuron networks/pathway at the system level requires the simultaneously recording and simulating behaviours from many sites in three-dimension (3D). Hence, great attentions have been focused on the fabrication of neural electrode arrays arranged in 3D structures [25]–[32]. Consequently, enormous amount of raw recording data from high density probe arrays normally demands preliminarily processing and filtering before further analyses [2]. Thus, the integration of complementary metal-oxide semiconductor (CMOS) circuits onto the microelectromechanical system (MEMS) fabricated silicon neural electrode probe becomes vitally important. Reports of successful on-chip integrations have been widely introduced, but most reported devices reply on complicated post-fabrication process [33]. In another word, the built-in integrated circuit is defined prior to the

Manuscript received December 5, 2014; revised March 6, 2015; accepted March 24, 2015. Date of publication April 13, 2015; date of current version September 29, 2015. This work was supported in part by the National Research Foundation (NRF) through Competitive research programme within the Self Powered Body Sensor Network for Disease Management and Prevention Oriented Healthcare Project under Grant R-263-000-A27-281, and in part by the NRF through the Competitive Research Programme (CRP) within the Peripheral Nerve Prostheses: A Paradigm Shift in Restoring Dexterous Limb Function Project under Grant R-719-000-001-281 and Grant NRF-CRP10-2012-01. Subject Editor Y. Zohar.

S. Zhang is with the Department of Electrical and Computer Engineering, National University of Singapore, Singapore 117576, and also with the Institute of Microelectronics, Agency for Science, Technology, and Research, Singapore 117685 (e-mail: elezss79@gmail.com).

S.-C. Yen and L.-D. Liao are with the Singapore Institute for Neurotechnology, National University of Singapore, Singapore 117456.

Z. Xiang and C. Lee are with the Department of Electrical and Computer Engineering, National University of Singapore, Singapore 117576.

D.-L. Kwong is with the Institute of Microelectronics, Agency for Science, Technology, and Research, Singapore 117685.

Color versions of one or more of the figures in this paper are available online at http://ieeexplore.ieee.org.

Digital Object Identifier 10.1109/JMEMS.2015.2417678

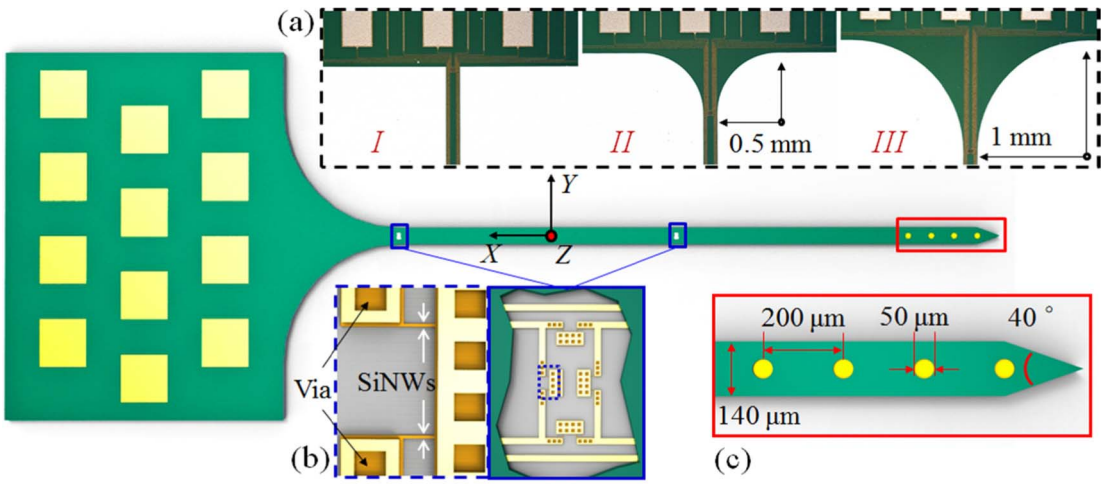

Fig. 1. The schematic of SiNWs embedded neural electrode probe. Inset (a) illustrates only the shape of probe base with three different designs (*I-III*). Inset (b) depicts four pairs of SiNWs configured in a Wheatstone bridge structure with a zoom-in of one pair. Inset (c) shows the layout of electrodes at tip.

fabrication of recording/simulation electrodes due to the process incompatibility (e.g. deposition and metallization of neural electrodes) between the standard CMOS fabrication and the sequential MEMS process.

Except a qualified interface between neuron and electrode along the probe, the device implantation mechanics is always pertaining to the final quality of recorded information [34]. During the probe implantation, optimization of tip, width, thickness and even insertion speed are crucial to reducing the tissue dimpling [35], [36] and the induced initial tissue damage [37], [38]. As a common practice to study the probe implantation behaviour, the traditional external load cell is connected to the base of the implantable device and perpendicular to the brain tissue surface [36]–[38]. However, the actual probe deformation is hard to be measured by feedback readings from load cell, especially when both torsion and bending mechanics are presented rather than a single factor [39]. Additionally, it is well known that the large mismatch in material properties (e.g. Si probe vs. brain tissue) would significantly escalate the tissue chronic response against the foreign body [10], [11], [40]. This common adopted hypothesis is established mostly based on FEM modelling [41]–[43] and separate measurement using bulky external device (e.g. DVRT) [44], [45]. The practical relationship between the loss/drift of recorded neural signal and variations of micro-motion has never been correlated due to the lack of experimental platform. It is thus necessary to explore such missing link using a single, integrated, implantable device with both recording and mechanical motion detection functions.

Based on the literature, it is possible to continually monitor a larger deformation of a beam structure by its strain changes till the complete structure fracture [46]. Taking advantage of the unique relationship between deformation and induced strain along probe shank, Najafi and Hetke [47] report the silicon probe with a single piezoresistive strain gauge embedded at the base of probe. The corresponding resistance change from the integrated polysilicon piezoresistor reflects the probe insertion mechanics. However, limited by the bulky geometry of polysilicon strain gauge, only a single piezoresistor is available in their prototype design. In addition, the absence of recording electrodes along the shank hinders the further exploration on micro-motion related neural signal fluctuations.

As one of the most promising nano-scale sensing elements [48]–[50], the successful demonstration of single crystal Si nanowires (SiNWs) in diverse applications has been widely reported (e.g. SiNW FETs [51]–[53], SiNW mechanical switches [54] and etc.). Moreover, dedicated researches on piezoresistance effect of single crystal silicon nanowires [56]–[58] suggest the feasibility of a better sensing performance by using SiNWs over traditional piezoresistive elements (e.g. metal strain gauge and doped polysilicon wires). Further implementations of SiNWs in NEMS piezoresistive sensors validate such theoretical possibility in various applications [59], [60].

II. Methods

A. Device Structure

In this paper, benefiting from the process compatibility by targeting different doping profiles on the same thin device silicon layer (initial thickness ~110nm), we introduce the Si electrode neural probe with built-in SiNWs strain sensors along the shank. The detailed device schematic is shown in Fig. 1. Two sets of SiNWs (highlighted in blue boxes along the shank) with moderate P-type doping level ($\sim 3.5 \times 10^{18}$ ion/cm^3) are fabricated at the middle and base of probe shank for the purpose of strain sensing. Full Wheatstone bridge structures (as indicated in inset (b) of Fig. 1) are applied for the direct voltage output with higher sensing resolution. At the probe tip, four highly P-doped silicon electrodes are defined in a diameter of 50 μm and a pitch of 200 μm (see inset (c) of Fig. 1). In addition, three different shapes of shank with various lengths (3, 5 & 7 mm) are designed (illustrated in inset (a) of Fig. 1) to verifying the strain sensing function of SiNWs regardless of the probe geometry variation. The buckling test will be discussed in the following section.

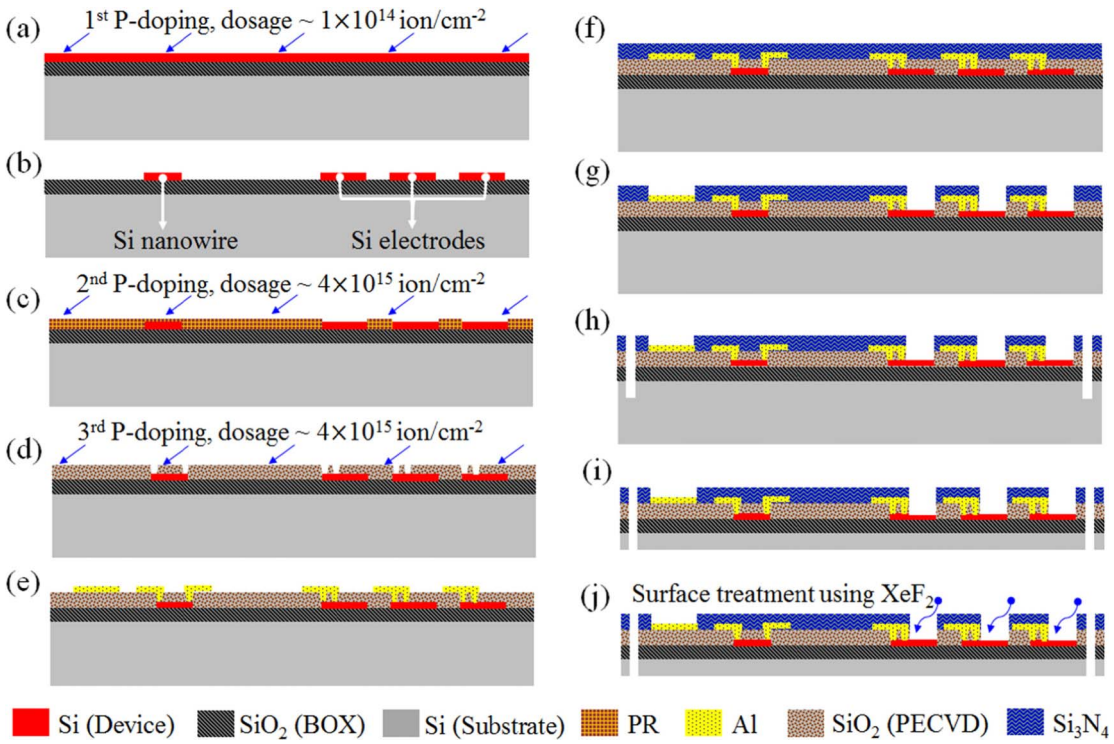

Fig. 2. Process flows of probe fabrications in sequences of (a) 1st global P-type implantation; (b) nanowire and electrodes patterning; (c) 2nd P-type implantation targeting only electrodes; (d) 3rd P-type implantation on via openings; (e) aluminum layer metallization; (f)-(g) deposition of low stress silicon nitride and electrode sites opening; (h) DRIE of the 60 μm trenches; (i) wafer backside grinding; (j) XeF_2 surface treatment.

Detailed fabrication steps of SiNWs embedded neural electrode probe is described as below.

B. Device Fabrication

8 inch (100) plane silicon on insulator (SOI) wafers (SOITEC; device silicon layer ~117 nm; buried thermal oxide (BOX) layer ~145 nm; nominal resistivity: 8.5 ~11.5 Ω cm) are used for device fabrications. As shown in Fig. 2(a), P-type dosage of 1×10^{14} ion/cm^2 is globally implanted with angle of 7° and twist of 22° at the beginning. 30 seconds rapid thermal annealing (RTA) at 1050 °C is then conducted for the dopant activation. The same step will also be conducted right after another two following implantations briefed in the later part. After photolithography and photoresist (PR) trimming process, both electrodes and SiNWs (with initial width of 110 nm along <110> direction) are defined on top of BOX layer (Fig. 2(b)). Further dry oxidation reduces the cross section of SiNWs below 100 nm. A TEM image of the final cross section is indicated Fig. 3(b). With the coverage of PR on rest areas, 2nd P-type implantation (dosage of 4×10^{15} ion/cm^2) is only focused on silicon electrodes as shown in Fig. 2(c). After deposition of 400 nm PECVD cladding layer and via openings, last P-type doping (dosage of 4×10^{15} ion/cm^2 is implanted to reduce the contact resistance between doped silicon and aluminum (Al) layers (Fig. 2(d)). Based on the resistance measured from testing kits, the estimated impurity carrier concentration is around 1×10^{20} cm^{-3} at both electrode and via regions. Aluminum is then metalized and covered by the following deposition of 1μm low stress silicon nitride (Si_3N_4)

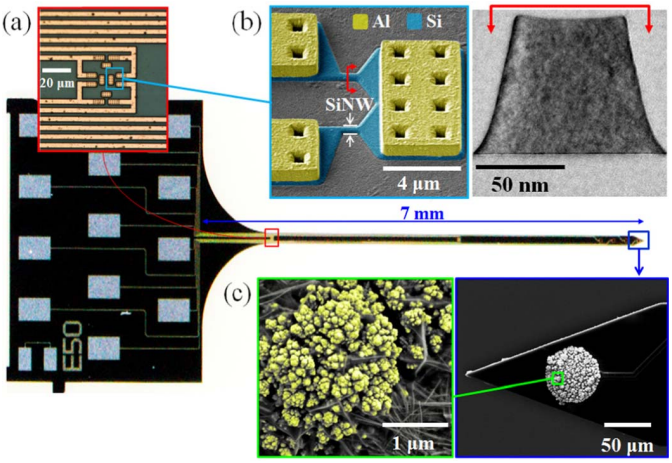

Fig. 3. (a) The optical image of a released probe device (design *II* with shank of 7 mm long). The inset indicates the layout of SiNWs strain sensor in Wheatstone bridge configuration. (b) A pair of SiNWs (highlighted in blue) after metallization of aluminum (highlighted in yellow). TEM cross-section is given in the inset. (c) SEM photo on tip of the probe device after electroplating process. The inset provides zoom-in SEM of coated electrode. Au nano-particles are highlighted as yellow dots.

as shown in Fig. 2(e)-(f)). A SEM picture of a pair of 1μm long SiNWs before deposition of nitride layer is given in Fig. 3(b). Sequentially, both bonding pads and electrode sites opening are defined through Reactive Ion Etching (RIE) processes (Fig. 2(g)). The shape of the probe is configured through the Deep Reactive Ion Etching (DRIE) down to 60 μm from the front side of wafer (Fig. 2(h)). The probe with

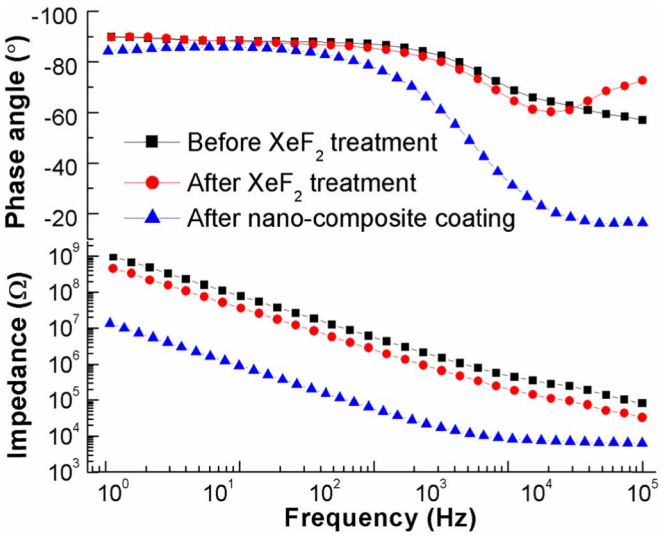

Fig. 4. Impedance spectroscopy plots of both phase (top) and interfacial impedance (bottom) changes with respect the frequency spanning from 100 KHz to 0.7 Hz. Typical impedances of silicon electrode at 1 KHz are recorded as 2.5 ± 0.4 MΩ (before XeF_2 treatment) and 0.9 ± 0.2 MΩ (after XeF_2 treatment). After deposition of CNTs & Au composites, the impedance drops by two orders (22 ± 3 KΩ) and the interfacial impedance indicates the nearly resistive behaviour at high frequency (100 to 10 KHz).

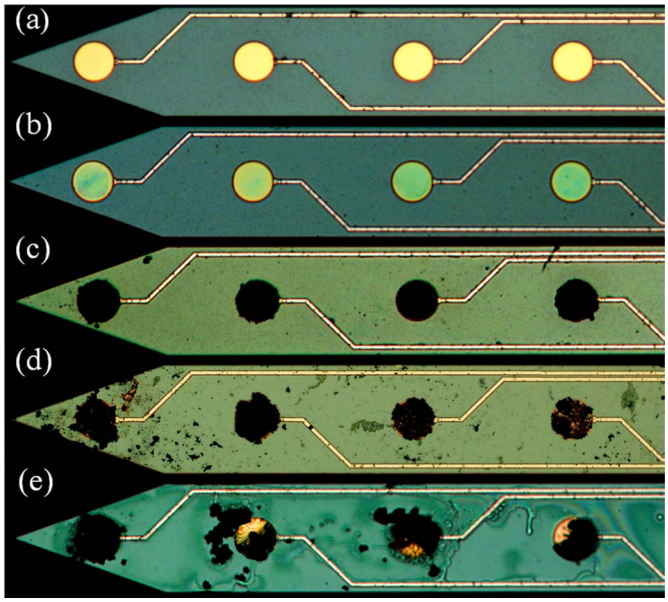

Fig. 5. The optical images of silicon electrodes under different stage: (a) before surface treatment; (b) after XeF_2 surface treatment; (c) after electroplating of nano-composites; (d) after 10 seconds of ultrasonic shake; (e) after twice implantation (insertion speed: 0.8∼1 mm/s) into rat brain.

an average thickness of 50 μm is released by the backside grinding (Fig. 2(i)). A sample image of final device (design *II* with shank of 7 mm long) is shown in Fig. 3(a) with the inset of the four pairs of SiNWs configured in full bridge structure. As the demonstration of a prototype for the silicon probe made by CMOS compatible processes, only single shaft design is presented, but the same process technique can be extended to the fabrication of an array of Si electrode probes.

C. Electrode Preparations

In order to facilitate the following deposition of nano-composite (CNTs + Au nanoparticles), Xenon difluoride (XeF_2) treatment on silicon electrode surface is carried out (∼2 seconds) in reticle level before the following electroplating process. After electroplating, the surface of silicon electrodes has been completely covered with MWCNTs and Au nanoparticles as shown in Fig. 3(c). As indicated in the SEM photo (shown in inset of Fig. 3(c)), the Au nanoparticles are highlighted in yellow dots, which are surrounded by fibrous-shaped CNTs. Please refer to our previous works for detailed electrode surface treatment [61] and electroplating processes [61], [62].

These additional composite coatings (CNTs + Au nanoparticles) on silicon electrodes significantly improve the total amount of ion transportations through the electrode-electrolyte interface, thus, a better charge storage capacity (CSC) [20] and a resultant lower noise level during recording. After the deposition, the improvement of CSC has been verified through electrochemical impedance spectroscopy (EIS) test. It is plotted in Fig. 4 that the typical interfacial impedance (at 1 KHz) has been improved by nearly two orders from 2.5 MΩ (before coating) to 22 KΩ (after coating). In addition, the impedance also tends to be more resistive at high frequency (>10 KHz) with deposited nano-composites on Si electrodes.

D. Electrode Surface Adhesion

Fig. 5(a) exhibits the optical image of highly doped silicon electrodes at the probe tips. After XeF_2 surface treatment, the color of electrodes turns into greenish (Fig. 5(b)). This is due to the slight exposure of the beneath BOX layer after creating a large amount of porosity on silicon layer. Mixture of MWCNTs (Cheap Tubes Inc., length ∼0.5-2 μm, outer diameter < 8 nm) into the Au electrolyte bath (TSG-250, Transene) is prepared inside a beaker. The optical photo on the probe tip after electroplating processes is provided in Fig. 5(c). With optimized electroplating parameter [61], nano-composites are conformably coated onto each electrode without a significant change of actual electrode area. The further adhesion test of composite coatings is firstly verified by ultrasonic shaking inside an ultrasonic cleaner (Branson B3510, 40 KHz, Max input power of 130 W). Surface coatings are able to survive even after 10 seconds ultrasonic shaking (shown in Fig. 5(d)). Nevertheless, the actual quality of the coating needs to be practically verified through *in vivo* implantation procedures. Fig 5(e) shows the image of the probe tip after twice implantations into rat brain. Partial delamination of coated patterns is observed for 3 out of 4 electrodes, but there no significant effects on electrode recording capability have been found. The insertion speed for the adhesion test is around 0.8∼1 mm/s, which will be considered as the fast insertion for an extreme case (high impact of friction force). Fast implantation of sharp devices normally results in lower mean effective strain and less vascular damages compared with slower insertions [35]–[37]. It is also suitable for screening a large number of animal experiments, but it takes risk of

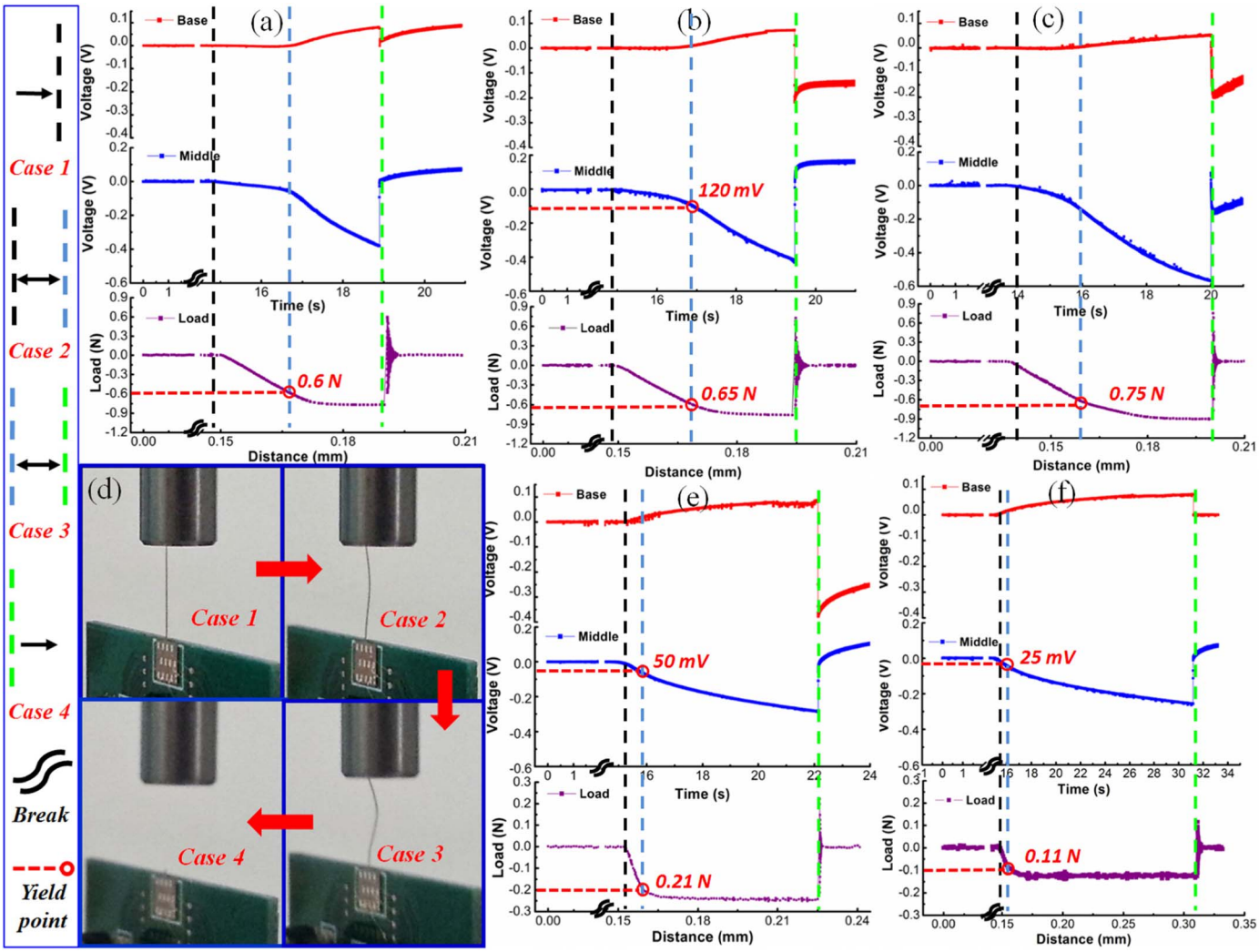

Fig. 6. Buckling tests of the probe with fixed probe length (3 mm) for (a) design *I*; (b) design*II*; (c) design *II;* and with fixed shank structure (design *II*) for different probe length of (e) 5 mm; (f) 7 mm. (d) shows snapshots of the probe under different *cases (1-4)* of buckling mechanics. The definition of the mechanical moment under each *case* is depicted on the left side of the figure (highlighted with the blue box).

the probe damage. Therefore, to extract clearer information of probe insertion mechanics, the implantation speed remains ~100 μm/s during the following *in vivo* test for the study of acute neural recording and even slower during the probe retraction (~10 μm/s).

III. Characterizations and Discussions

A. Mechanical Buckling Test

As aforementioned, there different mechanical geometry of probe base (shown in Fig. 1(a) for design *I*, *II* & *III*) and shank length (3, 5 & 7 mm) are designed to verify large influences on probe buckling and insertion behaviors. We first start buckling tests of silicon probes with the equal length (3 mm) but different shank designs in their base. Fig. 6(a) - (c) show mechanical buckling results of SiNWs probe with respect from design *I* to *III* in sequence. Red and blue curves demonstrate output changes recorded from SiNWs strain sensors located at base and middle of the shank, respective. The strain information is transferred and recorded as voltage outputs (as indicated in Fig.6) using National Instruments (NI) data acquisition system (NI USB-6363 and programed with Labview 2013). The testing is conducted under room temperature (25 °C) and the bridge circuit is biased with DC supply voltage of 2V. Readings (including both buckling force and displacement) from the load cell (Instron 2530-439, Maximum loading: ±5N, Resolution <0.25% of reading over static rating) are presented in purple curves.

Before the cylindrical fixture in contact with probe tip (*case 1*), all reading remains at their baseline. Right after the moment of contact between probes tip and fixture, readings from SiNWs strain sensors (both in base and middle of shank) and load cell change smoothly against the movement of cylindrical fixture (*case 2*). In another word, the relationship between buckling induced stress and strain is relatively linear and can be characterized by a constant factor (i.e. young's modules of the material) [39]. After load exceeding the critical buckling force or yield point (*case 3*), this linear relationship is no longer valid. Due to the presence of the torsion mechanism under large buckling, the reading from load cell tends to be

saturated even with a continuous external loading applied in cases of all three different shank designs. On the other hand, outputs of strain changes keep varying with the increasing external load till the probe breakage (*case 4*). Such non-linear relationship between applied loads and strain changes under a large buckling force tends to match the mechanical behavior of a silicon rod [46]. Hence, it is rather reasonable to monitoring the strain changes along the probe instead of loading forces in vertical direction. According to the literature [55] and our previous findings on piezoresistance effect of SiNWs under large strain changes [63], gauge factor of P-doped SiNWs in <110> direction can be close to 100 [57]. The value is at least doubled in contrast to the result of polysilicon piezoresistors reported from literature [47], thus, a better sensitivity of using SiNWs.

To further investigate the function of SiNWs strain sensors, buckling tests on probes with the same base structure (design *II* as defined in inset (a) of Fig.1) and various lengths (i.e. 3 mm, 5 mm and 7 mm) are also carried out and results are plotted in Fig. 5(b), (e) and (f). The saturation phenomenon of readings from load cell is even obvious for probe with longer shank. It can be concluded by the relationship between the maximum load/force (P) required to buckle the shank and other parameters related to probe geometry [37].

$$P = \frac{Ewt^3\pi^2}{6l^2} \tag{1}$$

Where w is the width, t is the thickness, l is the length and E is the Young's modulus. With fixed other geometric parameters, the longer probe results in a lower buckling force. It is also worth noting that voltage outputs from two SiNWs strain sensors change in opposite polarities, especially after external loads exceeding critical buckling forces. For the strain sensor at the base of shank (red plots in Fig. 6), the increment of output voltage can be explained by an overall resistance increase under a global tensile strain. As a result, probe shank physically bends towards to the device surface (Z direction as defined in Fig 1). Meanwhile, decreases of output voltage suggest that SiNWs suffer a global compressive strain at the middle of the probe. Hence, the probe shank bends downwards to the device surface (opposite to Z direction as defined in Fig. 1). Such extracted strain information matches probe mechanical behaviors captured in Fig. 6(d). Therefore, probe global bending mechanics can be precisely predicted based on the overall output changes. The detailed global strain analysis and the buckling mechanics will be extracted and discussed in the next.

B. Investigation of Strain and Buckling Load

Generally, the practical way of strain extraction can be realized through a multiplepoints bending setup [48]. Under such mechanical setup, the strain gauge usually will be attached onto the specimen surface for measuring the global strain changes due to the bending moment. The specimen could be in either a reticle or wafer level. The maximum applied strain with this approach is only up to 1% due to the limitation of such apparatus. Recently, with help of Raman spectroscopy to monitor the lattice changes, the localized strain information up to 4.5% has been reported [64]. However, both testing methods can not completely simulate the real situation of the probe buckling behavior (rather than simple mechanical bending) during implantation. Additionally, the physical dimension of the commercial strain gauge is usually in millimeter scale, which is an order larger than the physical geometry of our fabricated probe shank. It is thus not applicable to implement the strain gauge on the shank surface. The requirement of specimen preparations is also quite stringent for examining Raman peak shift. Not mention the difficulty of testing setup for the manipulation of the probe toward its mechanical fracture point during the Raman examination. Hence, as an alternative, we use the 3rd method – Finite element modeling (FEM) to simulate the global strain changes (not exact the localized strain) of the real case. However, the premise of running the simulation is to make sure the applied model matches the practical factor. For instance, a good agreement in term of the correlation for external loading and buckling mechanics should be firstly ensured between both FEM and measurement.

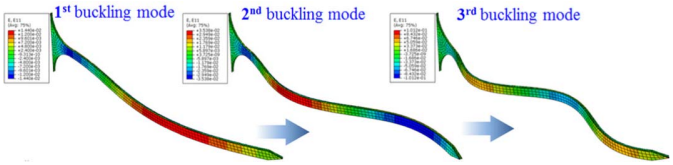

Fig. 7. Illustration for transitions of the buckling mode (from 1st to 3rd mode) simulated with the Finite Element Method (FEM).

FEM (*Abaqus 6.13*) modeling of probe buckling behaviors has been conducted based on a linear perturbation. During the simulation, you may increase the eigenvalue to high orders to obtain many possible probe deformation modes. Fig. 7 explains the mechanical behavior change between buckling modes (1st – 3rd mode) based on simulations. In the real buckling situation, the probe base starts bending at the 1st buckling mode (Referring to the point where red curve starts changing in Fig. 6). However, the buckling and strain sensitivity at the base is too small to capture the exact moment when the buckling starts. Meanwhile the fracture of Si probe will happen for further external loading beyond 3rd buckling mode. Therefore the mechanical strain at the middle of the probe after 1st buckling and before 2nd buckling mode becomes interested regions. After comparing the FEM result (loadings for the onset of 2nd buckling mode) with experimental data (exerted load at yield point), the simulated data is well matched with practical measurements. The comparison is tabulated in Table I and parameters used in FEM are summarized in Table II.

In addition, it can be also observed from experimental data (shown in Fig. 6) that the relationship between external loads and outputs from strain sensor (e.g. blue curve in Fig. 6) remains quite linear before reaching the yield point (or at the verge of entering 2nd buckling mode according to FEM). Since the probe design *II* will be used for the *in vivo* implantation (Details are discussed in Section *D*), we only extract corresponding voltage output from the strain sensor for design *II*. As a result, the consistent normalized sensitivity

TABLE I
COMPARISON BETWEEN MEASUREMENT DATA AND RESULTS FROM FEM

Probe Design		*I*	*II*			*III*
Probe Length		3mm	3mm	5mm	7mm	3mm
Measured Data	Exerted load at yield point (***N***)	*0.6*	*0.65*	*0.21*	*0.11*	*0.75*
	Voltage output at middle of probe (***mV***)	--	*120*	*50*	*25*	--
FEM	Load at the 2nd buckling mode (***N***)	*0.59*	*0.66*	*0.23*	*0.11*	*0.8*
	Average global strain at middle of probe (***%***)	*2.6*	*2.5*	*1.02*	*0.51*	*2.15*

TABLE II
MATERIAL PROPERTIES APPLIED IN THE FINITE ELEMENT METHOD (FEM)

Material	**Young's modulus**	**Poisson's ratio**	**Density (g/cm^3)**
Silicon	*170 GPa*	*0.28*	*2.329*

(∼24*mV/V/%*) for all three different lengths (3, 5 & 7mm) of probe is calculated based on information from Table I. However, this does not completely conclude detailed performance of individual sensing element (e.g. single SiNW), since the localized strain behavior may be more complicated than the global deformation or probe bending behavior. For example, the strain in longitudinal (*X-axis* defined in Fig. 1) and transverse (*Y-axis* defined in Fig. 1) directions will bring the opposite effects on total piezoresistance changes. Furthermore, to reduce the computational loading, the minimum element size used in FEMs is 10 μm and still 2orders larger than the critical dimension of SiNW in real case. Nevertheless, with this estimated sensitivity, we can deduce the probe penetration force and induced global strain during *in vivo* implantation. The detail will be discussed in Section *D* on probe mechanical response during the acute study.

C. In Vivo Recording

Male Sprague Dawley rats (Weight: 300 ∼330 g) are used for the *in vivo* study. Two craniotomies are carried at dorsal hippocampus CA1 region (2.0 mm lateral and 2.3 mm posterior to the bregma landmark) and somatosensory S1 region (2.5 mm lateral and 0.8 mm posterior to the bregma landmark), respectively. The former is used for the recording of neuron activities and the latter is only for monitoring mechanical behaviors. The probe is attached on the PCB and wire-bonded for electrical communications to NI data acquisition systems. Movements of the PCB in a vertical direction are manually controlled by the micromanipulator right on top of rat brain (e.g. CA1 or S1 regions). For neural recordings, brain signals are collected and amplified by RZ5D BioAmp Processor (Tucker-Davis Technologies, US). The insertion speed ranges from 0.1 to 1 mm/s for understanding insertion mechanics or neural recording purposes respectively. The final insertion depth is around 2.5 mm for probe implanted at both CA1 and S1 regions. Fig 8 (a) displays *in vivo* testing

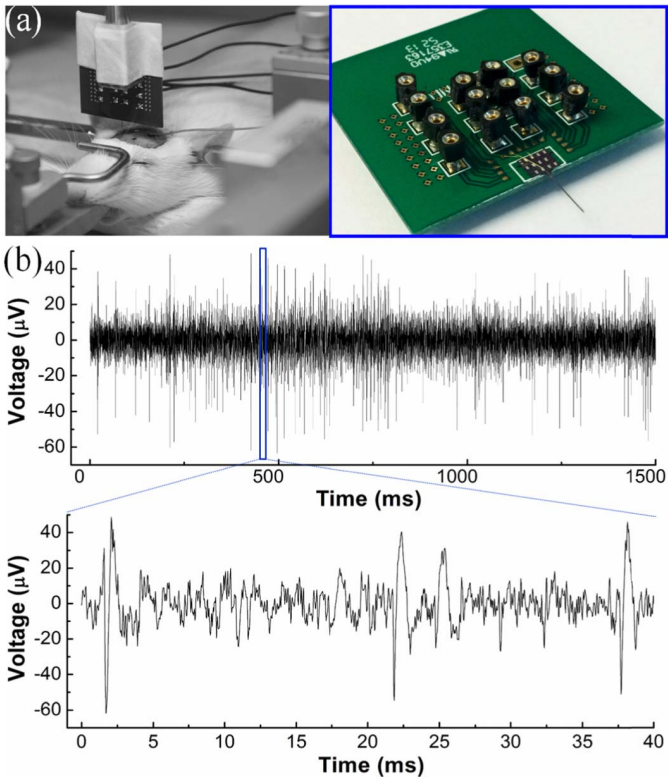

Fig. 8. (a) *In vivo* testing setups and a packaged Si-probe on PCB. (b) The plot of recorded neural signals with periods of 1.5 s and 40 ms (a zoom-in window) from CA 1 region of the Male Sprauge Dawley rat's brain.

setups with an inset showing a SiNWs probe after packaging. All testing procedures are performed under protocol 095/12(A3)13 and approved by the Institutional Animal Care and Use Committee at National University of Singapore. The rat is euthanized by overdose of CO_2 at the end of experiment.

Fig. 8(b) plots a segment of 1.5 seconds (at the top) and a 40 ms zoom-in view (at the bottom) from the continuous recording on brain signal. It has been reported that the action potential of central nerve system (CNS) is typically in the order of 100 μV, however, the signal strength may vary and be very subject to the proximity between electrode and the active neuron, thus, smaller amplitude of action potential is often detected [65]. Beside the signal amplitude, the background noise level is usually taken to judge the recording qualify of electrodes. In our measurement results, it is also worth noting that noise level is well controlled below 20 μV (calculated SNR >8), which is identical to the level reported from the electrode coated with other high charge composites (e.g. PEDOT/MWCNT) [18].

D. Acute Study on Recorded Mechanical Behaviours

The acute study is conducted with the probe design *II* (7mm long) and its insertion behavior is recorded in Fig. 9. With the aforementioned data acquisition system (Refer to Section III. *A*), blue and red plots represent signals recorded from SiNWs strain sensors embedded at the middle and base of the shank. As shown in Fig. 9(a), clear output glitches (highlighted in red dash box) indicate that probe is now

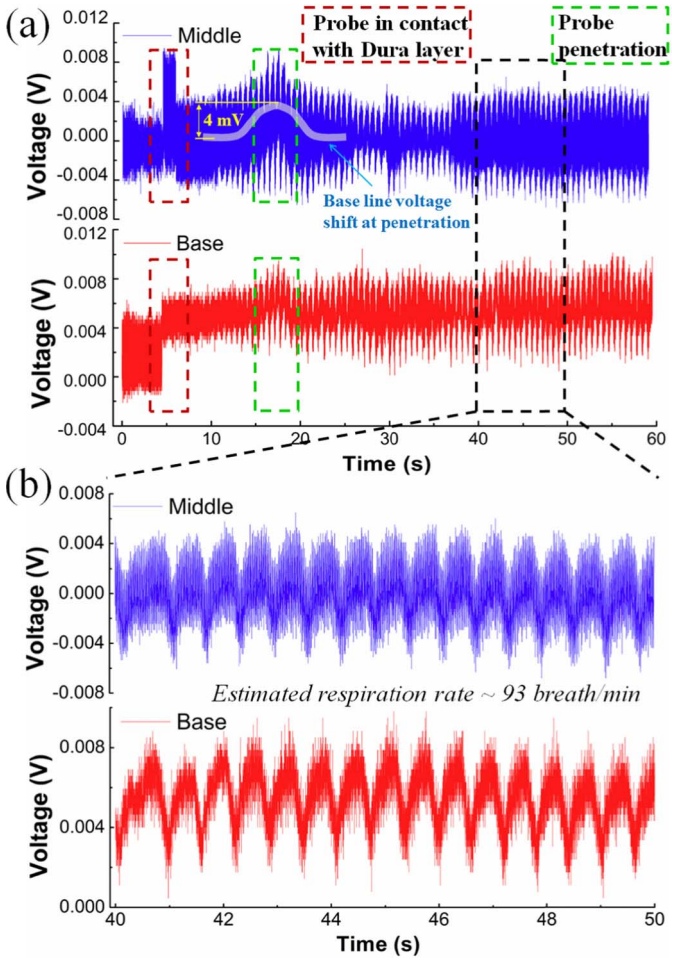

Fig. 9. (a) The plot of outputs from SiNWs strain sensors during *in vivo* probe insertions into rat's brain; and (b) a highlighted zoom-in period with spans of 10 seconds.

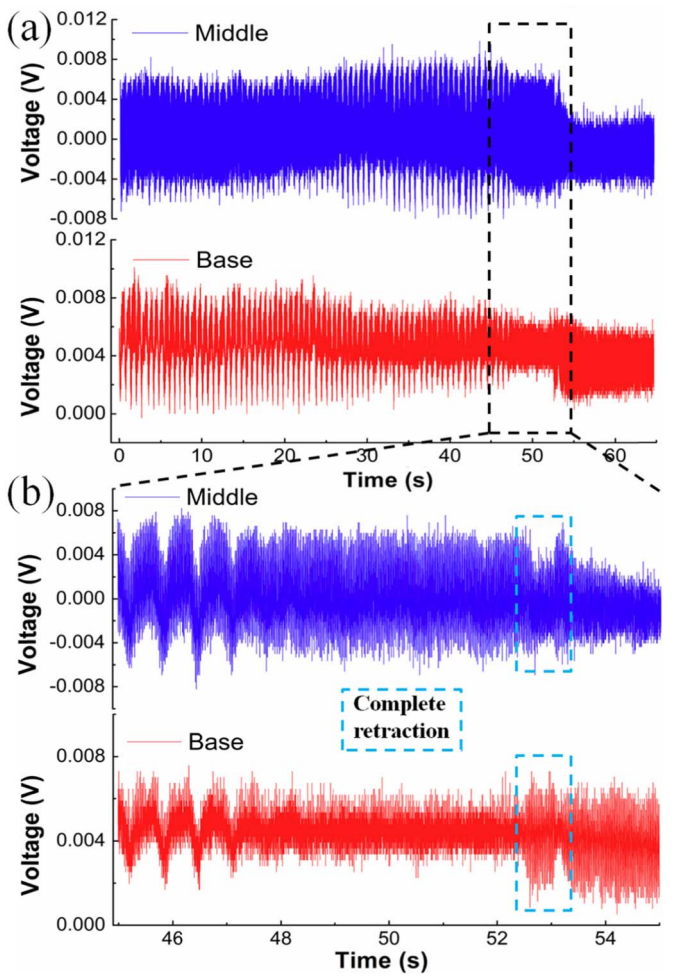

Fig. 10. (a) The plot of outputs from SiNWs strain sensors during *in vivo* probe retractions from rat's brain; and (b) a highlighted zoom-in period with spans of 10 seconds.

in contact with the brain tissue surface. Sequentially, the baseline voltage level gradually ramps up and down with the peak value occurring 10 seconds after the moment of contact. This explains that the moment of probe penetration inside brain tissue happens after the maximum tissue dimpling around 1 mm (given the insertion speed of 80 ~100 μm/s). In addition, with the information provided in Table I (At the yield point: load ~0.11N, strain ~0.51% and output from strain sensor ~25 mV) and the baseline voltage shift (~4 mV) shown in Fig. 9, both the penetration force (~18 mN) and induced global strain (~0.08%) at middle of probe can be estimated with the assumption of a linear mechanical strain and stress relationship, which is relatively true before reaching the yield point. The obtained penetration force (~18 mN) is in a good agreement with measurement data [34].

The vertical movement of the probe stops at the point of 35 seconds and this implies a total 2.5 mm final insertion depth. A zoom-in view (a period of 10 seconds indicated by the black dash box) is provided in Fig. 9(b) after 5 seconds break for tissue relaxations. According to the literature [44], the cycling spike signal is generated by the lateral micro-motion, which is possibly correlated to the respiratory behavior of the testing subject under different stage of anesthesia. Hence, information about the test subject's anesthesia status can be possibly deduced from status of its respiration rate (~93 breath/min). Since our primary goal is to demonstrate the function of micro-motion detection during the *in vivo* implantation, the detailed timing correlation between actual rat respirations and the micro-motions is not covered here.

The output information on the probe retraction is also depicted in Fig. 10(a) with a zoom-in period of 10 seconds (Fig. 10(b)) for a better view. The retraction speed is as slow as 10μm/s to ensure the complete tissue relaxation, hence, a better understanding of retraction mechanics. Retraction processes can be firstly monitored through the absence of cycling spikes, which disappear slightly before probe completely moving out of brain tissue surface. In addition, obvious glitches appear in plots of signals recorded from both the middle and base of shank at the moment of a complete probe retraction. The baseline signals are also restored to their original level (before probe in contact with brain tissue).

IV. Conclusion

By leveraging the fabrication compatibility and different doping profiles, both the neural electrodes and on-chip strain sensors are realized using the silicon device layer along probe shank. The charge transfer function of doped silicon

electrodes is verified and improved by further deposition of nano-composites (CNTs + Au nanoparticles). With lower interfacial impedance ($\sim$22 KΩ after electroplating), the noise level is properly contained (<20 μV) during the *in vivo* recording test on rat brain. Additionally, taking advantage of the great scalability of SiNWs, the built-in strain sensors configured in full bridge structures are embedded at middle and base of the shank for global strain sensing. The buckling experiment explores the consistent relationship between probe deformations and stain changes. Such relationship helps in revealing the clearer buckling mechanics of silicon probe till the complete fracture. With the superior sensitivity attributed from SiNWs strain sensors, further extracted strain information from acute study facilitates an accurate probe manipulation during the implantation procedure and also helps researcher understanding both *in vivo* mechanical and physiological behaviors (e.g. tissue penetration force and brain micro-motion). In summary, the proof-of-concept probe design offers an integrated platform, which can be applied to simultaneously study the correlation between electrical neural signal and reflected mechanical behavior in future chronic test.

REFERENCES

[1] H. HajjHassan, V. Chodavarapu, and S. Musallam, "NeuroMEMS: Neural probe microtechnologies," *Sensors*, vol. 8, no. 10, pp. 6704–6726, 2008.

[2] K. D. Wise, A. M. Sodagar, Y. Yao, M. N. Gulari, G. E. Perlin, and K. Najafi, "Microelectrodes, microelectronics, and implantable neural microsystems," *Proc. IEEE*, vol. 96, no. 7, pp. 1184–1202, Jul. 2008.

[3] L. Lin and A. P. Pisano, "Silicon-processed microneedles," *J. Microelectromech. Syst.*, vol. 8, no. 1, pp. 78–84, Mar. 1999.

[4] O. Frey *et al.*, "Biosensor microprobes with integrated microfluidic channels for bi-directional neurochemical interaction," *J. Neural Eng.*, vol. 8, no. 6, p. 066001, 2011.

[5] K. Seidl *et al.*, "In-plane silicon probes for simultaneous neural recording and drug delivery," *J. Micromech. Microeng.*, vol. 20, no. 10, p. 105006, 2010.

[6] O. Frey *et al.*, "Enzyme-based choline and L-glutamate biosensor electrodes on silicon microprobe arrays," *Biosensors Bioelectron.*, vol. 26, no. 2, pp. 477–484, 2010.

[7] J. Du, M. Roukes, and S. Masmanidis, "Dual-side and three-dimensional microelectrode arrays fabricated from ultra-thin silicon substrates," *J. Micromech. Microeng.*, vol. 19, no. 7, p. 075008, 2009.

[8] R. Biran, D. C. Martin, and P. A. Tresco, "Neuronal cell loss accompanies the brain tissue response to chronically implanted silicon microelectrode arrays," *Experim. Neurol.*, vol. 195, no. 1, pp. 115–126, 2005.

[9] R. Wang, W. Zhao, W. Wang, and Z. Li, "A flexible microneedle electrode array with solid silicon needles," *J. Microelectromech. Syst.*, vol. 21, no. 5, pp. 1084–1089, Oct. 2012.

[10] V. S. Polikov, P. A. Tresco, and W. M. Reichert, "Response of brain tissue to chronically implanted neural electrodes," *J. Neurosci. Methods*, vol. 148, no. 1, pp. 1–18, 2005.

[11] J. P. Seymour and D. R. Kipke, "Neural probe design for reduced tissue encapsulation in CNS," *Biomaterials*, vol. 28, no. 25, pp. 3594–3607, 2007.

[12] K. Seidl, S. Herwik, T. Torfs, H. P. Neves, O. Paul, and P. Ruther, "CMOS-based high-density silicon microprobe arrays for electronic depth control in intracortical neural recording," *J. Microelectromech. Syst.*, vol. 20, no. 6, pp. 1439–1448, Dec. 2011.

[13] Y.-T. Lee, S.-R. Yeh, Y.-C. Chang, and W. Fang, "Integration of silicon-via electrodes with different recording characteristics on a glass microprobe using a glass reflowing process," *Biosensors Bioelectron.*, vol. 26, no. 12, pp. 4739–4746, 2011.

[14] A. Béduer, P. Joris, S. Mosser, V. Delattre, P. C. Fraering, and P. Renaud, "Accurate resistivity mouse brain mapping using microelectrode arrays," *Biosensors Bioelectron.*, vol. 60, pp. 143–153, Oct. 2014.

[15] M. Tykocinski, Y. Duan, B. Tabor, and R. S. Cowan, "Chronic electrical stimulation of the auditory nerve using high surface area (HiQ) platinum electrodes," *Hearing Res.*, vol. 159, nos. 1–2, pp. 53–68, 2001.

[16] S. F. Cogan *et al.*, "Sputtered iridium oxide films for neural stimulation electrodes," *J. Biomed. Mater. Res. B, Appl. Biomater.*, vol. 89B, no. 2, pp. 353–361, 2009.

[17] Y. Su *et al.*, "The cytotoxicity of cadmium based, aqueous phase—Synthesized, quantum dots and its modulation by surface coating," *Biomaterials*, vol. 30, no. 1, pp. 19–25, 2009.

[18] S. Chen *et al.*, "PEDOT/MWCNT composite film coated microelectrode arrays for neural interface improvement," *Sens. Actuators A, Phys.*, vol. 193, pp. 141–148, Apr. 2013.

[19] H. Zhang, J. Shih, J. Zhu, and N. A. Kotov, "Layered nanocomposites from gold nanoparticles for neural prosthetic devices," *Nano Lett.*, vol. 12, no. 7, pp. 3391–3398, 2012.

[20] E. W. Keefer, B. R. Botterman, M. I. Romero, A. F. Rossi, and G. W. Gross, "Carbon nanotube coating improves neuronal recordings," *Nature Nanotechnol.*, vol. 3, pp. 434–439, Jun. 2008.

[21] J.-K. Wu, Y.-S. Wu, C.-S. Yang, and F.-G. Tseng, "Charge-selective gate of arrayed MWCNTs for ultra high-efficient biomolecule enrichment by nano-electrostatic sieving (NES)," *Biosensors Bioelectron.*, vol. 43, pp. 453–460, May 2013.

[22] C.-H. Chen *et al.*, "A flexible hydrophilic-modified graphene microprobe for neural and cardiac recording," *Nanomed., Nanotechnol., Biol., Med.*, vol. 9, no. 5, pp. 600–604, 2013.

[23] K. Najafi, K. D. Wise, and T. Mochizuki, "A high-yield IC-compatible multichannel recording array," *IEEE Trans. Electron Devices*, vol. 32, no. 7, pp. 1206–1211, Jul. 1985.

[24] G. Charvet *et al.*, "BioMEA: A versatile high-density 3D microelectrode array system using integrated electronics," *Biosensors Bioelectron.*, vol. 25, no. 8, pp. 1889–1896, 2010.

[25] K. Seidl, M. Schwaerzle, I. Ulbert, H. P. Neves, O. Paul, P. Ruther, "CMOS-Based High-Density Silicon Microprobe Arrays for Electronic Depth Control in Intracortical Neural Recording–Characterization and Application," *J. Microelectromech. Syst.*, vol. 21, no. 6, pp. 1426–1435, 2012.

[26] C.-W. Lin, Y.-T. Lee, C.-W. Chang, W.-L. Hsu, Y.-C. Chang, and W. Fang, "Novel glass microprobe arrays for neural recording," *Biosensors Bioelectron.*, vol. 25, no. 2, pp. 475–481, 2009.

[27] S. Spieth *et al.*, "A floating 3D silicon microprobe array for neural drug delivery compatible with electrical recording," *J. Micromech. Microeng.*, vol. 21, no. 12, p. 125001, 2011.

[28] K. Y. Kwon, B. Sirowatka, A. Weber, and W. Li, "Opto-μECoG array: A hybrid neural interface with transparent μECoG electrode array and integrated LEDs for optogenetics," *IEEE Trans. Biomed. Circuits Syst.*, vol. 7, no. 5, pp. 593–600, Oct. 2013.

[29] C.-H. Chen *et al.*, "A three-dimensional flexible microprobe array for neural recording assembled through electrostatic actuation," *Lab Chip*, vol. 11, no. 9, pp. 1647–1655, 2011.

[30] H.-C. Su *et al.*, "A cone-shaped 3D carbon nanotube probe for neural recording," *Biosensors Bioelectron.*, vol. 26, no. 1, pp. 220–227, 2010.

[31] R. Wang, X. Huang, G. Liu, W. Wang, F. Dong, and Z. Li, "Fabrication and characterization of a parylene-based three-dimensional microelectrode array for use in retinal prosthesis," *J. Microelectromech. Syst.*, vol. 19, no. 2, pp. 367–374, Apr. 2010.

[32] K. Y. Kwon, A. Weber, and W. Li, "Varying-length polymer microneedle arrays fabricated by droplet backside exposure," *J. Microelectromech. Syst.*, vol. 23, no. 6, pp. 1272–1280, Dec. 2014.

[33] C. Kim and K. D. Wise, "A 64-site multishank CMOS low-profile neural stimulating probe," *IEEE J. Solid-State Circuits*, vol. 31, no. 9, pp. 1230–1238, Sep. 1996.

[34] A. Sridharan, S. D. Rajan, and J. Muthuswamy, "Long-term changes in the material properties of brain tissue at the implant–tissue interface," *J. Neural Eng.*, vol. 10, no. 6, p. 066001, 2013.

[35] C. S. Bjornsson *et al.*, "Effects of insertion conditions on tissue strain and vascular damage during neuroprosthetic device insertion," *J. Neural Eng.*, vol. 3, no. 3, pp. 196–207, 2006.

[36] A. A. Sharp, A. M. Ortega, D. Restrepo, D. Curran-Everett, and K. Gall, "*In vivo* penetration mechanics and mechanical properties of mouse brain tissue at micrometer scales," *IEEE Trans. Biomed. Eng.*, vol. 56, no. 1, pp. 45–53, Jan. 2009.

[37] M. Welkenhuysen, A. Andrei, L. Ameye, W. Eberle, and B. Nuttin, "Effect of insertion speed on tissue response and insertion mechanics of a chronically implanted silicon-based neural probe," *IEEE Trans. Biomed. Eng.*, vol. 58, no. 11, pp. 3250–3259, Nov. 2011.

[38] A. Andrei, M. Welkenhuysen, B. Nuttin, and W. Eberle, "A response surface model predicting the *in vivo* insertion behavior of micromachined neural implants," *J. Neural Eng.*, vol. 9, no. 1, p. 016005, 2012.
[39] L. D. Landau and E. M. Lifshitz, *Theory of Elasticity* (Course of Theoretical Physics), vol. 5. New York, NY, USA: Pergamon, 1959.
[40] G. C. McConnell, T. M. Schneider, D. J. Owens, and R. V. Bellamkonda, "Extraction force and cortical tissue reaction of silicon microelectrode arrays implanted in the rat brain," *IEEE Trans. Biomed. Eng.*, vol. 54, no. 6, pp. 1097–1107, Jun. 2007.
[41] J. Subbaroyan, D. C. Martin, and D. R. Kipke, "A finite-element model of the mechanical effects of implantable microelectrodes in the cerebral cortex," *J. Neural Eng.*, vol. 2, no. 4, pp. 103–113, 2005.
[42] H. Lee, R. V. Bellamkonda, W. Sun, and M. E. Levenston, "Biomechanical analysis of silicon microelectrode-induced strain in the brain," *J. Neural Eng.*, vol. 2, no. 4, pp. 81–89, 2005.
[43] T. D. Y. Kozai *et al.*, "Mechanical failure modes of chronically implanted planar silicon-based neural probes for laminar recording," *Biomaterials*, vol. 37, pp. 25–39, Jan. 2015.
[44] A. Gilletti and J. Muthuswamy, "Brain micromotion around implants in the rodent somatosensory cortex," *J. Neural Eng.*, vol. 3, no. 3, pp. 189–195, 2006.
[45] M. Vähäsöyrinki, T. Tuukkanen, H. Sorvoja, and M. Pudas, "A minimally invasive displacement sensor for measuring brain micromotion in 3D with nanometer scale resolution," *J. Neurosci. Methods*, vol. 180, no. 2, pp. 290–295, 2009.
[46] C.-L. Hsin *et al.*, "Elastic properties and buckling of silicon nanowires," *Adv. Mater.*, vol. 20, no. 20, pp. 3919–3923, 2008.
[47] K. Najafi and J. F. Hetke, "Strength characterization of silicon microprobes in neurophysiological tissues," *IEEE Trans. Biomed. Eng.*, vol. 37, no. 5, pp. 474–481, May 1990.
[48] R. He and P. Yang, "Giant piezoresistance effect in silicon nanowires," *Nature Nanotechnol.*, vol. 1, no. 1, pp. 42–46, 2006.
[49] P. Neuzil, C. C. Wong, and J. Reboud, "Electrically controlled giant piezoresistance in silicon nanowires," *Nano Lett.*, vol. 10, no. 4, pp. 1248–1252, 2010.
[50] A. C. H. Rowe, "Piezoresistance in silicon and its nanostructures," *J. Mater. Res.*, vol. 29, no. 6, pp. 731–744, 2014.
[51] B. Sorée, W. Magnus, and W. Vandeberghe, "Low-field mobility in ultrathin silicon nanowire junctionless transistors," *Appl. Phys. Lett.*, vol. 99, no. 23, p. 233509, 2011.
[52] B. Sorée *et al.*, "Novel device concepts for nanotechnology: The nanowire pinch-off FET and graphene TunnelFET," *ECS Trans.*, vol. 28, no. 5, pp. 15–26, 2010.
[53] T. Wang, L. Lou, and C. Lee, "A junctionless gate-all-around silicon nanowire FET of high linearity and its potential applications," *IEEE Electron Device Lett.*, vol. 34, no. 4, pp. 478–480, Apr. 2013.
[54] Y. Qian, L. Lou, M. J. Tsai, and C. Lee, "A dual-silicon-nanowires based U-shape nanoelectromechanical switch with low pull-in voltage," *Appl. Phys. Lett.*, vol. 100, no. 11, p. 113102, 2012.
[55] J. S. Milne, I. Favorskiy, A. C. H. Rowe, S. Arscott, and C. Renner, "Piezoresistance in silicon at uniaxial compressive stresses up to 3 GPa," *Phys. Rev. Lett.*, vol. 108, p. 256801, Jun. 2012.
[56] T. Toriyama and S. Sugiyama, "Analysis of piezoresistance in p-type silicon for mechanical sensors," *J. Microelectromech. Syst.*, vol. 11, no. 5, pp. 598–604, Oct. 2002.
[57] T. Barwicz, L. Klein, S. J. Koester, and H. Hamann, "Silicon nanowire piezoresistance: Impact of surface crystallographic orientation," *Appl. Phys. Lett.*, vol. 97, no. 2, p. 023110, 2010.
[58] J. S. Milne, A. C. H. Rowe, S. Arscott, and C. Renner, "Giant piezoresistance effects in silicon nanowires and microwires," *Phys. Rev. Lett.*, vol. 105, no. 22, p. 226802, 2010.
[59] S. Zhang, L. Lou, and C. Lee, "Piezoresistive silicon nanowire based nanoelectromechanical system cantilever air flow sensor," *Appl. Phys. Lett.*, vol. 100, no. 2, pp. 023111-1–023111-3, 2012.
[60] S. Zhang *et al.*, "Annularly grooved diaphragm pressure sensor with embedded silicon nanowires for low pressure application," *J. Microelectromech. Syst.*, vol. 23, no. 6, pp. 1396–1407, Dec. 2014.
[61] S. Zhang *et al.*, "Development of silicon electrode enhanced by carbon nanotube and gold nanoparticle composites on silicon neural probe fabricated with complementary metal-oxide-semiconductor process," *Appl. Phys. Lett.*, vol. 104, no. 19, p. 193105, 2014.
[62] Z. Xiang *et al.*, "Ultra-thin flexible polyimide neural probe embedded in a dissolvable maltose-coated microneedle," *J. Micromech. Microeng.*, vol. 24, no. 6, p. 065015, 2014.
[63] L. Lou, W.-T. Park, S. Zhang, L. S. Lim, D.-L. Kwong, and C. Lee, "Characterization of silicon nanowire embedded in a MEMS diaphragm structure within large compressive strain range," *IEEE Electron Device Lett.*, vol. 32, no. 12, pp. 1764–1766, Dec. 2011.
[64] R. A. Minamisawa *et al.*, "Top-down fabricated silicon nanowires under tensile elastic strain up to 4.5%," *Nature Commun.*, vol. 3, Oct. 2012, Art. ID 1096.
[65] S. F. Cogan, "Neural stimulation and recording electrodes," *Annu. Rev. Biomed. Eng.*, vol. 10, pp. 275–309, Aug. 2008.

Songsong Zhang received the B.Tech. degree from the Department of Electrical and Computer Engineering, National University of Singapore, Singapore, in 2009, and the Ph.D. degree in electrical and computer engineering from the National University of Singapore, in 2014.

He is currently a Research Scientist with the Institute of Microelectronics, Agency for Science, Technology, and Research. His research interests include nanowire-based microelectromechanical systems, and nanoelectromechanical systems sensors and related biomedical applications.

Shih-Cheng Yen received the B.S.E., M.S.E., and Ph.D. degrees from the Department of Bioengineering, University of Pennsylvania, in 1993 and 1998, respectively. He is currently an Assistant Professor with the Department of Electrical and Computer Engineering, National University of Singapore. His research interests include neural coding, mechanisms underlying computation in the visual system, visual psychophysics, and biological models of the visual system.

Zhuolin Xiang received the B.Eng. degree from the Department of Information and Electronics, Beijing Institute of Technology, Beijing, China, in 2011. He is currently pursuing the Ph.D. degree in electrical and computer engineering with the National University of Singapore. His research interests focus mainly on BioMEMS devices for drug delivery and neural interfacing.

Lun-De Liao received the Ph.D. degree in electrical engineering from National Chiao Tung University (NCTU), Taiwan, in 2012. He was a Research Fellow with the Brain Research Center (BRC), NCTU. He proposed the world's first bioinspired dry Electroencephalogram sensors and their corresponding circuit to intelligently image the human brain under the guidance of Prof. C.-T. Lin (FIEEE) with BRC, NCTU. He was a Research Scientist with the Singapore Institute for Neurotechnology (SINAPSE), National University of Singapore, from 2012 to 2014. He is currently the Co-Founder of MINDO, a company for products in wearable and wireless electroencephalogram devices. He is a Senior Research Scientist and the Head of the Neurovascular Imaging Laboratory with SINAPSE. He has authored over 45 SCI peer-reviewed journal papers, and holds 11 patents. He was a recipient of the first place 2011 Young Investigator's Award from the World Association for Chinese Biomedical Engineers for his contributions on medical imaging and bioelectronics domain, and the 2012 Outstanding Research Award from NCTU for his outstanding research performance.

Dim-Lee Kwong (F'09) received the B.S. degree in physics and the M.S. degree in nuclear engineering from National Tsing Hua University, Hsinchu, Taiwan, in 1977 and 1979, respectively, and the Ph.D. degree in electrical engineering from Rice University, Houston, TX, in 1982. He was the Earl N. and Margaret Bransfield Endowed Professor with the University of Texas at Austin, from 1990 to 2007, and the Temasek Professor with the National University of Singapore, Singapore, from 2001 to 2004. He was the Founder of Rapro Technology Inc., in 1986, and Micro Integration Corporation, in 1988, and has been a Consultant to government research laboratories, semiconductor IC manufacturers, and materials and equipment suppliers in the U.S. and overseas. He is currently an Executive Director of the Institute of Microelectronics (IME) with the Agency for Science, Technology, and Research, Singapore; a Professor of Electrical and Computer Engineering with the National University of Singapore; and an Adjunct Professor of Electrical and Computer Engineering with the University of Texas at Austin. He has authored over 1000 refereed archival publications (560 journal and 470 conference proceedings), has presented more than 80 invited talks at international conferences, and holds 25 U.S. patents. As an Executive Director of IME, he develops and implements IME's multidisciplinary and multifaceted research and development strategy, and research programs that are substantially driven by commercial applications as the end goal. He leads interdisciplinary teams of semiconductor technology, photonics, bioscience, radio frequency and mixed-signal IC design, and advanced packaging, together with strategic industrial and clinical partners, to develop leading-edge disruptive technologies for Si photonics, green electronics, 3-D IC, microelectromechanical systems, and biomedical applications. He was a recipient of the IBM Faculty Award from 1984 to 1986, the Semiconductor Research Corporation Inventor Awards from 1993 to 1994, the General Motor Foundation Fellowship from 1992 to 1995, the Halliburton Foundation Excellent Teaching Award in 1994, the Engineering Foundation Award in 1995, and the IEEE George Smith Award in 2007. He was also a recipient of the IEEE Frederik Philips Award with the following citation for leadership in silicon technology and excellence in the management of microelectronics research and development in 2011.

Chengkuo Lee (S'93–M'96) received the M.S. degree in materials science and engineering from National Tsing Hua University, Hsinchu, Taiwan, in 1991; the M.S. degree in industrial and system engineering from Rutgers University, New Brunswick, NJ, in 1993; and the Ph.D. degree in precision engineering from the University of Tokyo, Tokyo, Japan, in 1996. He was a Foreign Researcher with the Nanometer Scale Manufacturing Science Laboratory, Research Center for Advanced Science and Technology, University of Tokyo, from 1993 to 1996. He was with the Mechanical Engineering Laboratory, AIST, MITI, Japan, as a JST Research Fellow, in 1996. Thereafter, he became a Senior Research Staff Member with the Microsystems Laboratory, Industrial Technology Research Institute, Hsinchu. In 1997, he joined Metrodyne Microsystem Corporation, Hsinchu, and established the Microelectromechanical Systems (MEMS) Device Division and the first micromachining fab for commercial purposes in Taiwan. He was the Manager of the MEMS Device Division from 1997 to 2000. He was an Adjunct Assistant Professor with the Electrophysics Department, National Chiao Tung University, Hsinchu, in 1998, and the Institute of Precision Engineering, National Chung Hsing University, Taichung, Taiwan, from 2001 to 2005. In 2001, he co-founded Asia Pacific Microsystems, Inc., where he first became the Vice President of Research and Development, before becoming the Vice President of the Optical Communication Business Unit, and a Special Assistant to the Chief Executive Officer in charge of international business and technical marketing for the MEMS foundry service. From 2006 to 2009, he was a Senior Member of the Technical Staff with the Institute of Microelectronics, Agency for Science, Technology, and Research, Singapore. He is currently an Associate Professor with the Department of Electrical and Computer Engineering, National University of Singapore, Singapore. He has co-authored the books *Advanced MEMS Packaging* (McGraw-Hill, 2010), and *Micro and Nano Energy Harvesting Technologies* (Artech House, 2014). He has contributed to more than 240 international conference papers and extended abstracts, and 170 peer-reviewed international journal articles in sensors, actuators, energy harvesting, MEMS, nanoelectromechanical systems, metamaterials, nanophotonics, and nanotechnology. He holds nine U.S. patents.